


Experimental study on the stability and breakup of a planar liquid sheet under a standing wave acoustic field

Boqi Jia,¹ Tiehan Wang ,^{2,3} Qing-fei Fu,^{3,4,*} and Li-jun Yang^{3,4}

¹*Institute of Combustion and Thermal Systems, School of Mechanical, Electronic and Control Engineering, Beijing Jiaotong University, Beijing 100044, China*

²*Shanghai Space Propulsion Technology Research Institute, Shanghai 201109, China*

³*School of Astronautics, Beihang University, Beijing 100083, China*

⁴*Aircraft and Propulsion Laboratory, Ningbo Institute of Technology, Beihang University, Ningbo 315800, China*

 (Received 4 August 2022; accepted 13 December 2022; published 29 December 2022)

When combustion instability occurs—in addition to periodic change in the nozzle flow rate caused by pressure oscillation—the instability of the liquid sheet is also affected by pressure oscillation, reflected mainly in oscillation of the internal parameters of the fluid. In this work, the parametric instability of a liquid sheet under a standing wave acoustic field was studied theoretically, and the influence of acoustic parameters on the instability of a liquid sheet was analyzed. It was found that sinuous and varicose modes were coupled in the subharmonic region. Atomization characteristics of slit nozzles under a standing wave acoustic field were studied experimentally; the effects of acoustic pressure and injector position were analyzed with respect to the acoustic field on atomization characteristics and the characteristics of nozzles in the critical state. It was found that under the same acoustic pressure, the effect of the acoustic field at the velocity antinode (VAN) was stronger than the effect at the acoustic intensity antinode (IAN), and there was little effect at the acoustic pressure antinode. There was also a critical value of acoustic pressure: when the pressure threshold was exceeded, Faraday waves were motivated at VAN and IAN. An interesting phenomenon is that the frequency of the surface wave is the same as the acoustic frequency, but the Faraday wave was found to be subharmonic rather than harmonic. The effect of flow rate on atomization characteristics was analyzed. The wavelength of the Faraday wave and breakup length of the liquid sheet were well in accord with the theoretical wavelength calculated in the analysis of liquid sheet instability.

DOI: [10.1103/PhysRevFluids.7.124004](https://doi.org/10.1103/PhysRevFluids.7.124004)

I. INTRODUCTION

Combustion instability is a major technical problem that must be considered in the development of rocket engines. Its main characteristic is that pressure oscillation in the combustion chamber is consistent with the intrinsic acoustic mode of the combustion chamber, leading to the instantaneous change of local heat release [1], which often causes engine damage, or even explosion. To control this instability, it is necessary to understand the mechanism of combustion instability resulting from the local transient heat release rate. Atomization is an important link in the combustion process, as well as the oscillation of pressure manifested as the fluctuation of the acoustic field. Many experimental studies have shown that the oscillation of the acoustic field greatly influences fluid atomization and, when the acoustic field is strong enough, it may change the form of the

*fuqingfei@buaa.edu.cn

atomization. Redistribution of the spray also plays an important role in combustion instability, making examination of the atomization process under acoustic disturbance significantly important.

Current research focuses mainly on atomization of the jet nozzle and the liquid droplets in the acoustic field, but atomization of a liquid sheet in the acoustic field has been less studied. During experimental study of atomization of a liquid sheet in an acoustic field, two main installation modes exist for the nozzle: one method is to make the injection direction parallel to the acoustic field, and the other is to make it perpendicular to the acoustic field. In an experiment with nozzle injection parallel to the acoustic field, Rhys [2] studied the breakup of a liquid sheet under acoustic excitation. The experimental results showed that the amplitude of disturbance on the surface of the liquid sheet increased with the decrease in frequency of the acoustic field, and the frequency of breakup was the same as the frequency of the acoustic field.

Sivadas *et al.* [3,4] measured the atomization of an air-assisted liquid sheet in the acoustic field, using water as the working medium; the optimal frequency to break the liquid sheet was observed. The parameters of the critical amplitude of disturbance, breakup length, and breakup time of the liquid sheet were analyzed and compared with those without an acoustic field. Results showed that during atomization the disturbance of an acoustic field can overcome gravity and surface tension. Therefore, when the Weber number was small, the surface waves were more regular, making it possible to control the initial stage of liquid sheet atomization.

Siegler *et al.* [5] studied the atomization characteristics of a slit nozzle in the parallel acoustic field. They analyzed the oscillation frequency of a liquid sheet with acoustic oscillation and revealed the relationship between the two oscillation frequencies. The sudden change of oscillation frequency of the liquid sheet was also observed under specific working conditions.

In an experiment with a spraying nozzle perpendicular to an acoustic field, Sujith [6] observed the interaction between the spray and the acoustic field, using alcohol as the working medium. His experiment showed that an intensive acoustic field can reduce the length of the spray field. The spray velocity field was measured by the particle image velocimetry (PIV) method, and the droplet velocity decreased notably under acoustic vibration, indicating the formation of smaller droplets. Sujith inferred that the acoustic velocity affected the spray field more directly than the acoustic pressure.

Mulmule *et al.* [7] studied instability and atomization characteristics of a liquid sheet formed by an impinging nozzle in a vertical acoustic field. When the acoustic pressure was lower than the acoustic pressure threshold for a given frequency, there was no oscillation on the liquid surface, but when the acoustic pressure was higher than the threshold, the acoustic field had an obvious effect on the liquid sheet. The acoustic pressure threshold increased with the increase of the acoustic frequency. In addition, the liquid sheet displayed an obvious response to some specific frequencies, and those frequencies changed with variation in the Weber number of the liquid sheet. The response of the liquid sheet to acoustic vibration was measured by the extended length of the liquid sheet. It was found that lower frequency had a stronger effect on the liquid sheet; at the same time, atomization was improved.

Dighe and Gadgil [8] examined the breakup dynamics of a liquid sheet in a vertical acoustic field. Their experiment revealed the phenomenon of the acoustic field causing a violent swing of the liquid sheet, resulting in the decrease of the breakup length and width of the liquid sheet and increasing amplification of the impact wave. In subsequent studies [9], the authors discovered that beyond a certain frequency the liquid sheet did not respond to acoustic vibration, and the cutoff frequency was an increment of the Weber number. This was similar to the results obtained by Mulmule [7], but it should be noted that Dighe and Gadgil believed that parameter resonance could not dominate the breakup process of a high-speed liquid sheet in an acoustic field, and that Kelvin-Helmholtz instability was the main reason for the breakup process. Only when the Weber number is small, can parameter oscillation be found on a liquid sheet.

Air-assisted atomization of a jet nozzle under a high-frequency standing wave acoustic field has been widely studied [10–14], and the jet flattening phenomenon at pressure nodes of the acoustic chamber observed. Faraday waves were also found on the surface of the flat liquid sheet. It was believed that at the pressure node, nonlinear radial acoustic pressure crushed the jet into a flat liquid

sheet, which atomized rapidly after formation. There are three atomization phenomena: the natural breakup mode of the liquid sheet, Faraday instability, and membrane breakup. After the fracture of the liquid sheet, and under the effect of radial acoustic force, the droplet converges toward the pressure node.

Rhys [2] conducted preliminary experimental research on the atomization characteristics of slit nozzles in the transverse standing wave acoustic field. Photographs were taken of the liquid sheet generated by the slit nozzle in the standing wave acoustic field in the direction of the sheet's extension. It was observed that the liquid sheet was more unstable in the oscillating acoustic field than in the steady state without an acoustic field. Breakup of the liquid sheet was observed in the sinuous mode at the acoustic pressure node. Rhys [2] also observed that many droplets appeared on the surface of the liquid sheet when the nozzles were placed at the pressure antinode; the liquid sheet was also more unstable than the steady state, which Rhys believed to be caused by the squeezing effect of the acoustic field on the liquid sheet. All these results indicated that the redistribution of spray in the engine may have caused combustion instability.

In these studies, much of the research that included oscillating acoustic fields was introduced; Faraday waves were observed in some of the studies—causing the parametric instability. Parametric instability is the instability of a certain parameter of the basic fluid flow, periodically changing with time. Fundamentally, it is Rayleigh-Taylor (RT) instability [15] and Kelvin-Helmholtz (KH) instability [16] when the stability of the basic flow is transferred to the unsteady basic flow [17,18], and the parametric oscillation of the basic flow causes the instability driving force (inertia force, aerodynamic force, etc.) to change periodically. In the entire cycle, the work done by the driving force of instability is greater than that of the dissipative force, leading to the occurrence of instability. Parametric instability is a major influence on the ultrasonic atomization of fluid [19] and the atomization of fuel in the combustor with a pressure oscillation field [10]. Therefore, in this work, the introduction of parametric instability is very important to the study of the atomization mechanism.

Faraday [20] first conducted a systematic experimental study on the parametric instability of fluid. He observed that surface waves were generated by fluid interfaces of a flume in the vertical direction, usually in the form of standing waves. It was found that the oscillation frequency of the fluid interface was half that of the flume's oscillating frequency. These surface fluctuations, caused by oscillations, are known as Faraday waves.

Mulmule [7] studied the parametric instability in a plane liquid sheet, formed by impinging nozzles in the transverse acoustic field, and he established the physical model of the liquid sheet under the acoustic field. Mulmule believed that when the acoustic pressure generated by the acoustic field displayed vertical effects on the liquid sheet, the main effect on sheet instability was velocity oscillation generated by pressure oscillation. By converting acoustic pressure to vertical velocity oscillation, he obtained the dispersion equation of a liquid sheet under transverse velocity oscillation, and the parametric instability was analyzed. However, in that study, the experiment was conducted in an open environment with a traveling wave acoustic field, so the study of liquid sheet instability in a standing wave acoustic field is still awaiting resolution.

To investigate the atomization characteristics of slit nozzles under the transverse standing wave acoustic field, parametric instability was conducted first, to find the dispersion relation of the liquid sheet and predict the length of the Faraday wave. The atomization experiment of slit nozzles under the transverse standing wave acoustic field was then conducted. The effects of acoustic pressure amplitude, injector position with respect to acoustic field, and liquid Weber number of the nozzle on the atomization characteristics were then analyzed. The length of the Faraday wave obtained on the liquid sheet surface was compared with the predicted wavelength in a parametric instability theory.

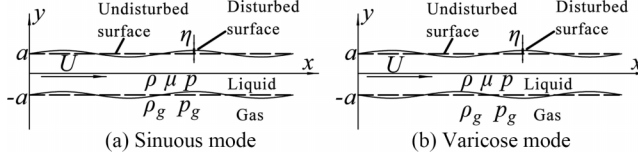


FIG. 1. Schematic of physical model of liquid sheet disturbance.

II. INSTABILITY OF LIQUID SHEET UNDER A STANDING WAVE ACOUSTIC FIELD

The liquid sheet is considered to be located at the velocity antinode of the acoustic field. Compared with the static gas environment, the liquid sheet is subjected to gas velocity oscillation that is perpendicular to its liquid surface, and velocity oscillation will bring oscillating normal stress to its boundary. The liquid sheet will display accelerated movement, and that is the oscillation term affected by the acoustic field. In addition, at any position except the pressure antinode, the liquid sheet receives oscillation of the pressure gradient from the acoustic field, because the acoustic pressure on both sides of the liquid sheet is different. But at the pressure antinode, the acoustic pressure on both sides of the liquid sheet is equal, so the effect of the acoustic field on its instability is far less than at any other position, consistent with the experimental phenomenon. Therefore, the effect of the acoustic field on the liquid sheet can be expressed by normal acceleration oscillation in its instability analysis.

A. Dispersion equations

It was assumed that the plane liquid sheet was viscous, the gas on both sides was inviscid, both gas and liquid were incompressible, and the surrounding gas was static when it was not disturbed. The disturbance was two-dimensional and it existed in the flow direction, perpendicular to the boundary, as shown in Fig. 1. The liquid sheet thickness is $2a$, the density is ρ , the dynamic viscosity is μ , and the surface tension is σ . The basic flow without disturbance is constant flow with velocity U in the x direction; the disturbance velocity in the x and y directions is u and v , and the disturbance pressure is p . The gas density above and below the liquid sheet is ρ_g , the disturbance velocities in the x and y directions are u_g and v_g , respectively, and the disturbance pressure is p_g . For the sinuous mode, the perturbations of both upper and lower surfaces are η .

In our earlier theoretical study [21], the dispersion relation of the linear instability of a liquid sheet in a transverse standing acoustic field was obtained. However, the sinuous and varicose modes were decoupled in that study [21]. In the present research, the coupling of sinuous and varicose modes is taken into consideration.

The process of conducting the governing equation can be found in Fang *et al.* [21]; the governing equations of the liquid sheet are obtained at $-a < y < a$:

$$\frac{\partial u}{\partial x} + \frac{\partial v}{\partial y} = 0, \quad -a < y < a, \quad (2.1)$$

$$\rho \left(\frac{\partial u}{\partial t} + U \frac{\partial u}{\partial x} \right) = -\frac{\partial p}{\partial x} + \mu \left(\frac{\partial^2 u}{\partial x^2} + \frac{\partial^2 u}{\partial y^2} \right), \quad -a < y < a, \quad (2.2)$$

$$\rho \left(\frac{\partial v}{\partial t} + U \frac{\partial v}{\partial x} \right) = -\frac{\partial p}{\partial y} + \mu \left(\frac{\partial^2 v}{\partial x^2} + \frac{\partial^2 v}{\partial y^2} \right), \quad -a < y < a, \quad (2.3)$$

$$v = \frac{\partial \eta}{\partial t} + U \frac{\partial \eta}{\partial x}, \quad y = \pm a, \quad (2.4)$$

$$\frac{\partial u}{\partial y} + \frac{\partial v}{\partial x} = 0, \quad y = \pm a, \quad (2.5)$$

$$\frac{\partial^2 \phi_g}{\partial x^2} + \frac{\partial^2 \phi_g}{\partial y^2} = 0, \quad y < -a \quad \text{or} \quad y > a, \quad (2.6)$$

$$p_g = -\rho_g \frac{\partial \phi_g}{\partial t}, \quad y < -a \quad \text{or} \quad y > a, \quad (2.7)$$

$$v_g = \frac{\partial \eta}{\partial t}, \quad y = \pm a, \quad (2.8)$$

$$-p + 2\mu \frac{\partial v}{\partial y} - \sigma \frac{\partial^2 \eta}{\partial x^2} + p_g - (\rho_g - \rho)g \cos(\omega t)\eta = 0, \quad y = a, \quad (2.9)$$

$$-p + 2\mu \frac{\partial v}{\partial y} + \sigma \frac{\partial^2 \eta}{\partial x^2} + p_g - (\rho_g - \rho)g \cos(\omega t)\eta = 0, \quad y = -a, \quad (2.10)$$

$$\phi_g \rightarrow 0, \quad p_g \rightarrow 0, \quad y \rightarrow \infty. \quad (2.11)$$

Equations (2.1)–(2.11) are linear equations to be solved for the dispersion relation. Because they have been linearized, and are all partial differential equations with respect to x and t , allowing the solution of the equation to have the harmonic form, the parameters can be written as

$$(u, v, p, \phi_g, p_g) = [u_n(y), v_n(y), p_n(y), \phi_{gn}(y), p_{gn}(y)] \exp(ikx + \beta t)F(t), \quad (2.12)$$

where k is wave number and β is the Floquet exponent. Addressing the temporal mode, that is the same growth rate of all points in space. So k is a real number, and $\beta = \beta_r + i\beta_i$ is a complex number; its actual part β_r represents the growth rate of the disturbance, and its imaginary part β_i represents the frequency of fluctuations. $F(t)$ is a period in time with period $1/f$ and may therefore be expanded in a Fourier series:

$$F(t) = \sum_{n=-\infty}^{+\infty} \exp(in\omega t), \quad \omega = 2\pi f, \quad (2.13)$$

where f is the frequency of the acoustic field.

Note that the sinuous and varicose modes should be taken into consideration because there may be coupling between the two modes:

$$\eta^+ = \eta^I + \eta^{II}, \quad \eta^- = \eta^I - \eta^{II}, \quad (2.14)$$

$$\eta^\pm = \eta_o^\pm \exp(ikx + \beta t)F(t) = \sum_{n=-\infty}^{+\infty} \eta_n^\pm \exp(ikx + \beta t + in\omega t), \quad (2.15)$$

where η^I and η^{II} are the displacements of the upper and lower surface, respectively. Therefore, η^- is the thickness of the liquid sheet varying spatially and temporally.

Using the above formulas, the dispersion equation can be obtained:

$$A_{1n}\eta_n^+ = B(\eta_{n+1}^- + \eta_{n-1}^-), \quad A_{2n}\eta_n^- = B(\eta_{n+1}^+ + \eta_{n-1}^+), \quad (2.16)$$

where

$$A_{1n} = \frac{\mu}{\rho} (l_n^2 + k^2) [\rho(\omega_{en} + ikU) + 2\mu k^2] \tanh(ka) - 4 \frac{\mu^2 k^3 l_n}{\rho} \tanh(l_n a) + \sigma k^3 + \rho_g \omega_2,$$

$$A_{2n} = \frac{\mu}{\rho} (l_n^2 + k^2) [\rho(\omega_{en} + ikU) + 2\mu k^2] \coth(ka) - 4 \frac{\mu^2 k^3 l_n}{\rho} \coth(l_n a) + \sigma k^3 + \rho_g \omega_{en}^2,$$

$$B = -\frac{(\rho - \rho_g)gk}{2},$$

$$\begin{aligned}\omega_{en} &= \beta + in\omega, \\ l_n^2 &= k^2 + \frac{\rho}{\mu}(\omega_{en} + Uik).\end{aligned}\tag{2.17}$$

Finally, the dispersion matrix can be obtained as

$$\mathbf{A}_1\boldsymbol{\eta}^+ = \mathbf{B}\boldsymbol{\eta}^-, \quad \mathbf{A}_2\boldsymbol{\eta}^- = \mathbf{B}\boldsymbol{\eta}^+, \tag{2.18}$$

where

$$\begin{aligned}\mathbf{A}_1 &= \begin{pmatrix} \ddots & \vdots & \vdots & 0 & 0 & 0 & 0 \\ \cdots & A_{1-2} & 0 & 0 & 0 & 0 & 0 \\ \cdots & 0 & A_{1-1} & 0 & 0 & 0 & 0 \\ 0 & 0 & 0 & A_{10} & 0 & 0 & 0 \\ 0 & 0 & 0 & 0 & A_{11} & 0 & \cdots \\ 0 & 0 & 0 & 0 & 0 & A_{12} & \cdots \\ 0 & 0 & 0 & 0 & \vdots & \vdots & \ddots \end{pmatrix}, \\ \mathbf{A}_2 &= \begin{pmatrix} \ddots & \vdots & \vdots & 0 & 0 & 0 & 0 \\ \cdots & A_{2-2} & 0 & 0 & 0 & 0 & 0 \\ \cdots & 0 & A_{2-1} & 0 & 0 & 0 & 0 \\ 0 & 0 & 0 & A_{20} & 0 & 0 & 0 \\ 0 & 0 & 0 & 0 & A_{21} & 0 & \cdots \\ 0 & 0 & 0 & 0 & 0 & A_{22} & \cdots \\ 0 & 0 & 0 & 0 & \vdots & \vdots & \ddots \end{pmatrix}, \\ \mathbf{B} &= \begin{pmatrix} \ddots & \vdots & \vdots & 0 & 0 & 0 & 0 \\ \cdots & 0 & B & 0 & 0 & 0 & 0 \\ \cdots & B & 0 & B & 0 & 0 & 0 \\ 0 & 0 & B & 0 & B & 0 & 0 \\ 0 & 0 & 0 & B & 0 & B & \cdots \\ 0 & 0 & 0 & 0 & B & 0 & \cdots \\ 0 & 0 & 0 & 0 & \vdots & \vdots & \ddots \end{pmatrix}, \\ \boldsymbol{\eta}^+ &= (\cdots \quad \eta_{-2}^+ \quad \eta_{-1}^+ \quad \eta_0^+ \quad \eta_1^+ \quad \eta_2^+ \quad \cdots)^T, \\ \boldsymbol{\eta}^- &= (\cdots \quad \eta_{-2}^- \quad \eta_{-1}^- \quad \eta_0^- \quad \eta_1^- \quad \eta_2^- \quad \cdots)^T.\end{aligned}$$

Note that $A_{10} = 0$ and $A_{20} = 0$ are the dispersion equations of a planar viscous liquid sheet in a steady inviscid gas medium. However, these two equations are coupled in the present study, indicating that the sinuous and varicose modes inevitably coexist. For instance, if there is only sinuous mode, there should be $\boldsymbol{\eta}^- = \mathbf{0}$, and $\mathbf{A}_1\boldsymbol{\eta}^+ = \mathbf{B}\boldsymbol{\eta}^-$ becomes $\mathbf{A}_1\boldsymbol{\eta}^+ = \mathbf{0}$. As a result, the effect of acoustic oscillations in \mathbf{B} cannot act on the computed result. Therefore, $\boldsymbol{\eta}^+$ and $\boldsymbol{\eta}^-$ are both nonzero.

B. Results discussion

Figure 2 is displayed to explain the unstable mechanism of the surface wave. There are no acoustic oscillations in Figs. 2(a)–2(c). $\beta = \beta_r + i\beta_i$ is the complex growth rate, where β_r is the growth rate and β_i is the frequency. As plotted in Fig. 2(a), there is only one solution of β_i when $\beta_r > 0$, and there are two branches of β_i (β_{i1} and β_{i2}) when $\beta_r < 0$. For convenience to analyze the surface wave composed by β_{i1} and β_{i2} , the reference system can be transferred to move with the liquid sheet axially, as shown in Fig. 2(b). The two branches of β_i represent a pair of traveling

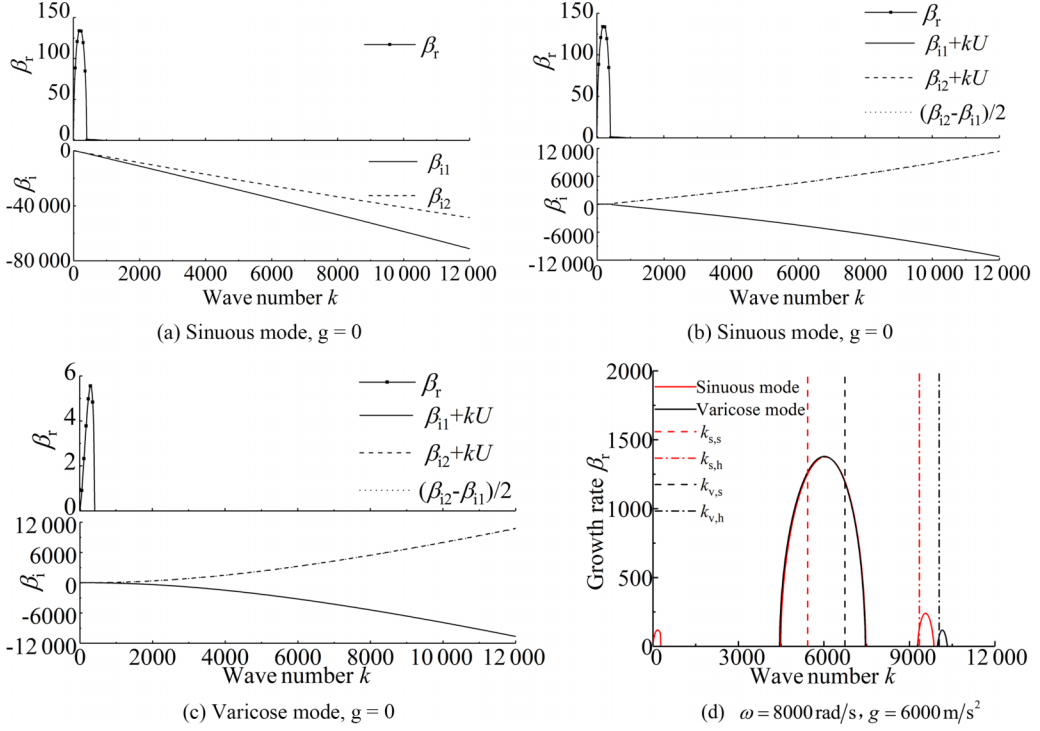


FIG. 2. Instability of the liquid sheet in different cases. (a)–(c) Growth rate (upper figure) and frequency (lower figure) of the planar liquid sheet in the steady gas medium; (a) sinuous mode; (b) sinuous mode in the reference system moving with the liquid sheet; (c) varicose mode in the reference system moving with the liquid sheet; (d) growth rate of a planar liquid sheet in the presence of acoustic oscillations. ($\rho = 1000 \text{ kg/m}^3$, $\mu = 0.001 \text{ Pa s}$, $\sigma = 0.073 \text{ Pa m}$, $a = 0.00015 \text{ m}$, and $U = 5 \text{ m/s}$.)

waves as below:

$$\cos(kx + \beta_{i1}t + kUt) + \cos(kx + \beta_{i2}t + kUt) = \cos\left(kx + \frac{\beta_{i1} + \beta_{i2}}{2}t + kUt\right) \cos\left(\frac{\beta_{i1} - \beta_{i2}}{2}t\right). \quad (2.19)$$

Note that $\beta_{i1} + kU \approx -(\beta_{i2} + kU)$, so the surface wave in Eq. (2.19) is approximately a standard standing wave, $\cos(kx)\cos[(\beta_{i1} - \beta_{i2})t/2]$. Therefore, this standing wave can be regarded as the natural mode of the surface wave for a certain wave number k , and $(\beta_{i1} - \beta_{i2})/2$ can be regarded as the inherent frequency. Similarly, the inherent frequency of the natural mode of the varicose mode can also be found, as shown in Fig. 2(c). Under the acoustic oscillation, the natural mode will be motivated when the frequency of the natural mode satisfies $(\beta_{i1} - \beta_{i2})/2 = n\omega/2$, $n = 1, 2, 3, \dots$, will be motivated when the acoustic oscillation is introduced. Therefore, the corresponding wave numbers of the natural modes with inherent frequencies $n\omega/2$ are exhibited in Fig. 2(d), where $k_{s,s}$, $k_{s,h}$, $k_{v,s}$ and $k_{v,h}$ represent the wave numbers corresponding to inherent frequencies $\omega/2$ and ω of sinuous and varicose modes, respectively. It can be found in Fig. 2(d) that more than one unstable region appears. Similar to Figs. 2(b) and 2(c), the first unstable region is due to KH instability, which is motivated by the relative velocity between liquid and gas phases. However, in this region, the dispersion curve of the varicose mode disappears, while the dispersion curve of the sinuous mode still exists. The second unstable region

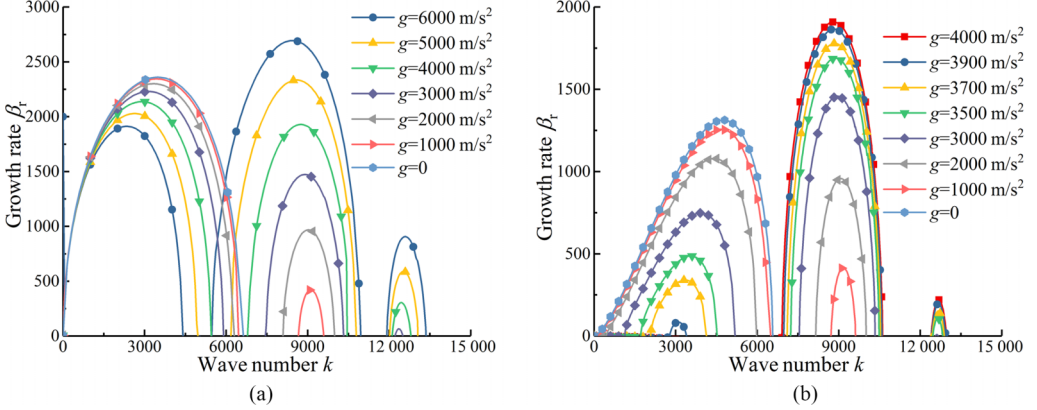


FIG. 3. Effect of oscillation amplitude on the instability of (a) sinuous and (b) varicose modes. ($\rho = 1000 \text{ kg/m}^3$, $\mu = 0.001 \text{ Pa s}$, $\sigma = 0.073 \text{ Pa m}$, $a = 0.00015 \text{ m}$, $U = 20 \text{ m/s}$, and $\omega = 8000 \text{ rad/s}$.)

locates around $k_{s,s}$ and $k_{v,s}$. Because the oscillating frequency of the surface wave in this region is half of the acoustic frequency, this region is called the subharmonic region. It can be found that there is only one subharmonic region; in other words, the subharmonic regions of the sinuous and varicose modes coincide. In addition, the dominant wave number of this region locates between $k_{s,s}$ and $k_{v,s}$. The reason is that in Eq. (2.18), the sinuous and varicose modes couple with each other. It is found that at the dominate wave number, the frequency is about 3400 and 4600 rad/s, respectively. Meanwhile, 4600 and 3400 rad/s are inherent frequencies of sinuous and varicose modes at this wave number, respectively. The simplest expression to qualitatively understand this coupling effect is as follows:

$$\cos(kx) \cos(3400t) + \cos(kx) \cos(4600t) = 2 \cos(kx) \cos(600t) \cos(4000t). \quad (2.20)$$

Equation (2.20) displays the coupling effect of the sinuous and varicose modes. Although Eq. (2.20) is not a standard form of standing wave, it also establishes a waveform that may be motivated by the parametric instability. For this reason, there is only one subharmonic region. However, the third unstable regions, i.e. the harmonic regions, are separate for sinuous and varicose modes. Moreover, it can be found that the subharmonic region is the most unstable.

Figure 3 displays the effect of oscillation amplitude on the instability of sinuous and varicose modes. With the increase of oscillation amplitude, the subharmonic and harmonic regions are both enlarged, but the KH unstable region diminishes. The KH unstable region of the varicose mode is more sensitive to the oscillating amplitude. When $g = 4000 \text{ m/s}^2$, the KH unstable region of the varicose unstable mode disappears. However, the KH unstable region still exists when $g = 6000 \text{ m/s}^2$. Moreover, the dominant wave number in the subharmonic and harmonic regions is almost unchanged with the increase of oscillating amplitude.

Figure 4(a) exhibits the dispersion curve which corresponds to the typical cases of the experiments in Sec. IV. It can be found that the subharmonic region is the most unstable. Because the liquid-to-gas velocity is too small, the KH unstable region at small wave numbers is not found. Moreover, due to the viscous dissipation, the harmonic regions are stable. It can be found in Fig. 4(b) that with the increase of oscillating amplitude, the growth rate in the subharmonic region increases from negative to positive value. There must be a critical oscillating amplitude g_{cr} making the maximum growth rate equal to 0. g_{cr} is a significant parameter to determine the relation between g and the sound pressure, which will be elaborated upon in Sec. IV.

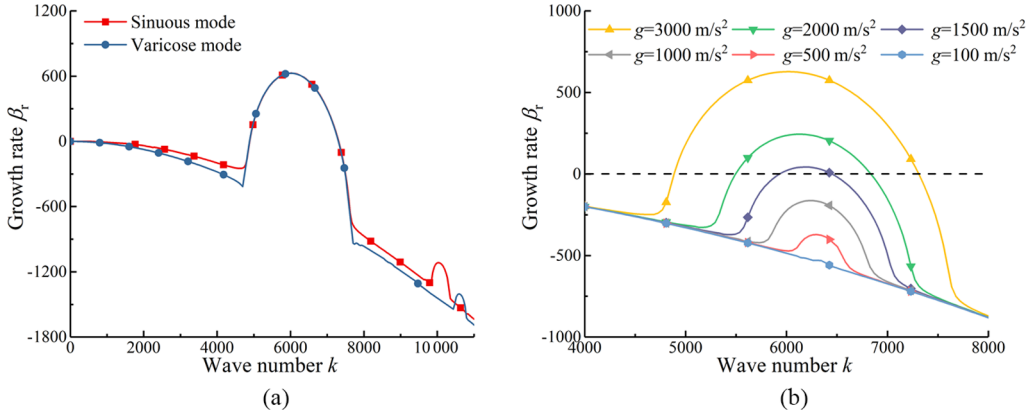


FIG. 4. Dispersion curves of typical working conditions of the experiment in Sec. IV. (a) Comparison between sinuous and varicose modes; (b) effect of oscillation amplitude. ($\rho = 1153.8 \text{ kg/m}^3$, $\mu = 0.011 \text{ Pa s}$, $\sigma = 0.0688 \text{ Pa m}$, $a = 0.00015 \text{ m}$, $U = 1.5 \text{ m/s}$, $g = 3000 \text{ m/s}^2$, and $f = 1200 \text{ Hz}$.)

III. EXPERIMENT SETUP

A. Experiment system

The experimental system shown in Fig. 5 consisted of an atomization system and a measurement system. The atomization system included the pump pressure system, liquid pipeline, signal generator, power amplifier, high-frequency loudspeaker, acoustic chamber, and the nozzle module. In the acoustic chamber, there was a transverse standing wave oscillating acoustic field, generated by high-frequency loudspeakers. The liquid that formed the liquid sheet was a glycerin-water

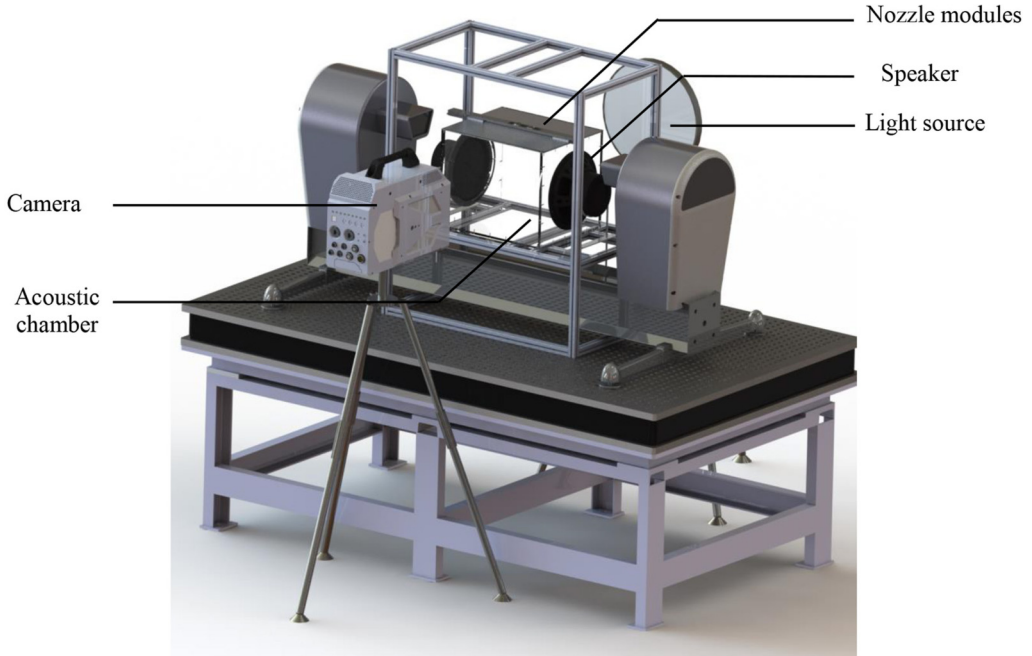


FIG. 5. Experimental system diagram.

TABLE I. Experimental conditions.

Number	Mass fraction of the solution	Flow rate (g/s)	We_l
1	60%	10.5	10.82
2	60%	12.6	11.52
3	60%	14.7	13.86

solution. The measurement system included computer, high-speed camera, data acquisition card, Coriolis force flowmeter, microphone, light source, and a laser particle analyzer. In the experiment, a UTG2062A signal generator created a sine wave signal, and a BNB A-1800 power amplifier boosted the signal; Beyma CP-850Nd drivers were used to produce the acoustic field, which was measured by BSWA MPA401 and MPA421 microphones, and sampled by a DH5922N data acquisition card (20 000 samples per second). Microphones estimated the acoustic signal measured by the microphones at different positions with respect to the acoustic field and adjusted the output frequency of the signal generator to produce the transverse standing wave acoustic field. A Photron SA-Z high-speed camera (20 000 fps) was used to measure the spray field; the shooting direction of the camera was perpendicular to the liquid sheet.

The experimental conditions were systematic (Table I) in order to obtain the atomization characteristics of the nozzle with the influence of parameters such as acoustic pressure, nozzle position with respect to the acoustic field, and nozzle flow rate. Three different nozzle flow rates, and the atomization characteristics of the nozzle under each flow rate, were analyzed with nine different acoustic pressures, ranging from 0 to 8000 Pa, and three different nozzle positions: the pressure antinode (PAN), intensity antinode (IAN), and velocity antinode (VAN). When comparing working conditions one, two, and three, the liquid Weber number We_l was used to evaluate the basic aerodynamic forces, because atomization was strongly linked to the thickness of the liquid sheet generated by the slit nozzle.

The liquid Weber number is defined as

$$We_l = \rho_l U_0^2 2a / \sigma, \quad (3.1)$$

where $2a$ is the thickness of the liquid sheet generated by the slit nozzle.

The dimension of the slit nozzle is 20 mm \times 1 mm. In Table I, the liquid density and viscosity are 1153.8 kg/m³ and 10.96 mPa s, respectively. The gas density and the surface tension are 1.2 kg/m³ and 68.8 mN/m, respectively.

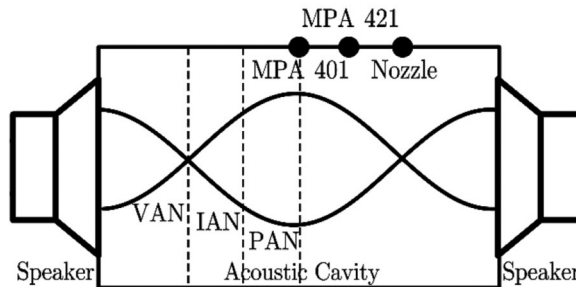


FIG. 6. Diagram of acoustic field distribution and microphone position in acoustic chamber.

B. Measurement of acoustic field and calibration of microphone

As shown in Fig. 6, the acoustic pressure distribution of the acoustic field in the chamber was obtained by using two microphones to measure the signal change of the acoustic pressure at two positions in the chamber, with time.

First the form of the acoustic field was assumed to be [22]

$$p(x, t) = A_+ e^{ik_{s+}x + i\omega_s t} + A_- e^{-ik_{s-}x + i\omega_s t}. \quad (3.2)$$

In the linear acoustic field, A_+ , A_- , k_{s+} , k_{s-} , and ω_s are the amplitude and wave number of the acoustic wave propagating forward and backward, and the frequency of the acoustic wave, respectively. Acoustic waves traveling forward and backward had the same frequency. The wave number was obtained with the following formula:

$$k_{s+} = k_s / (1 + M), \quad (3.3)$$

$$k_{s-} = k_s / (1 - M), \quad (3.4)$$

where $k_s = \omega/c$ and M is the Mach number of the average airflow velocity. In this work, the velocity of the gas in the chamber caused by the speakers was much less than the amplitude of the oscillating velocity, so it was simplified as

$$k_{s+} = k_{s-} = k. \quad (3.5)$$

Therefore, the pressure at the measured position was expressed as

$$p(x_i, t) = \text{Re}(a_i e^{i\varphi_i + i\omega_s t}), \quad (3.6)$$

where

$$a_i e^{i\varphi_i} = A_+ e^{ikx_i} + A_- e^{-ikx_i}. \quad (3.7)$$

At present, the unknown quantities are A_+ and A_- ; therefore, they can be obtained through the acoustic pressure data of two points, as follows:

$$F \mathbf{z} = \mathbf{b}, \quad (3.8)$$

where

$$\mathbf{z} = \begin{bmatrix} A_+ \\ A_- \end{bmatrix}, \quad \mathbf{b} = \begin{bmatrix} a_1 e^{i\varphi_1} \\ a_2 e^{i\varphi_2} \end{bmatrix}, \quad F = \begin{bmatrix} e^{ikx_1} & e^{-ikx_1} \\ e^{ikx_2} & e^{-ikx_2} \end{bmatrix}. \quad (3.9)$$

At this point, distribution of the entire acoustic field was obtained through the signal of the microphone; the sensitivity of the microphones was calibrated by exchanging their measuring positions in the same acoustic field. The assumption was that the spatial distribution of the acoustic field was stable under the same frequency, and that acoustic pressure did not affect the spatial distribution form or the relative proportion at each position. The sensitivity of microphone 1 was G_1 ; the sensitivity of microphone 2 was G_2 . The signals measured for the first and the second time are represented by the superscript ' and '' respectively. The voltage at two points (A and B), was measured by microphones 1 and 2 in the first measurement; the position of the microphones was exchanged in the same acoustic field in the second measurement. Because of the stable distribution of the acoustic field, the acoustic pressure amplitude measured by the two microphones was

$$p'_a = V'_1 / G_1, \quad p'_b = V'_2 / G_2, \quad (3.10)$$

$$p_a'' = V_2''/G_2, \quad p_b'' = V_1''/G_1, \quad (3.11)$$

where V represents the voltage amplitude measured by the microphone, and p represents the local acoustic pressure amplitude. Due to the stable spatial distribution of acoustic field, we have

$$\frac{p_a'}{p_a''} = \frac{p_b'}{p_b''}. \quad (3.12)$$

By substituting (3.10) and (3.11) into (3.12), it was found that the sensitivity ratio of the two microphones was

$$\frac{G_1}{G_2} = \sqrt{\frac{V_1'V_1''}{V_2'V_2''}}. \quad (3.13)$$

The advantage of this method was that it reduced system error, because, after opening the speakers several times, a change of parameters could occur (such as impedance), even at the same input voltage; the output amplitude of the speakers also changes. This method decreased this type of error.

C. Production of the transverse standing wave acoustic field

To generate a standing wave acoustic field in the experiment and ensure the nozzle enough space to adjust between the pressure antinode and the velocity antinode of the acoustic field, the wavelength of the excited acoustic field was maintained exactly equal to the axial length of the acoustic chamber, that is, the first-order transverse oscillation mode excited in the acoustic chamber. Therefore, the speaker frequency f was set to

$$f = \frac{c}{L}, \quad (3.14)$$

where c is the speed of sound and L is the axial length of the acoustic chamber. Compared to the nearby frequency range, in this acoustic mode the acoustic pressure amplitude measured by the two microphones was the largest, and it had the same phase. In fact, temperature changes affected the resonant frequency of the chamber by affecting the speed of sound. In the experiment the acoustic frequency was around 1150 Hz; this frequency was searched and corrected before beginning each experiment. Figure 7 shows the acoustic pressure signal measured by two microphones in the experiment. Figure 8 shows the spectrum diagram obtained after Fourier transform. It can be seen from Figs. 7 and 8 that the main frequency of the acoustic pressure signal was 1216 Hz—close to the frequency of the speakers. Therefore, it can be presumed that a first-order oscillating standing wave acoustic field with a wavelength equal to the axial length of the acoustic chamber was generated.

IV. ATOMIZATION CHARACTERISTICS OF A SLIT NOZZLE IN A TRANSVERSE STANDING WAVE ACOUSTIC FIELD

In this section the atomization characteristics of a slit nozzle in a transverse standing wave acoustic field are expressed; the effect of acoustic pressure amplitude, nozzle positions, and liquid Weber number are discussed; the effects on atomization characteristics (including critical pressure p_{cr} , wavelength of Faraday wave λ and oscillating frequency f , nozzle characteristic length L_c , and expansion angle θ of liquid sheet) are examined. In addition, the wavelength and oscillating frequency of Faraday wave obtained from the experiment are compared with the theory in Sec. II.

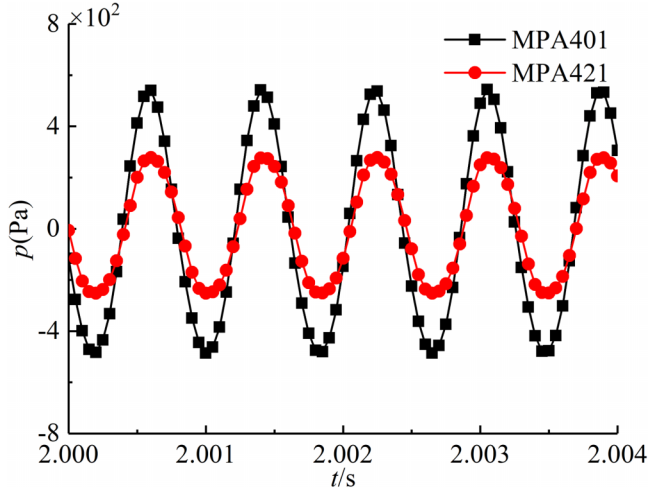


FIG. 7. Acoustic pressure measured by microphones.

A. Effects of acoustic pressure amplitude and nozzle position

All experiments were conducted under the experimental conditions of No. 1, shown in Table I. Figure 9 shows the atomization images at VAN under different p_{ac} . p_{ac} was the peak-to-peak acoustic pressure measured at PAN. As shown in Fig. 9, in the definition of θ , when the edge of the liquid sheet converged inward, θ was negative; when the edge of the liquid sheet expanded outward, θ was positive. L_c is defined as the distance from the nozzle exit to the impacting point of the liquid sheet edge, before the sheet broke (p_{ac} at 0–4000 Pa), or the breakup length of the nozzle (p_{ac} at 5000–8000 Pa). Figure 9 shows that the influence of the acoustic field on the atomization characteristics of the liquid sheet formed by the slit nozzle was reflected mainly in the change of the expansion angle and in the characteristic length of the liquid sheet and the generation of the Faraday wave on the liquid sheet surface.

In the theory analysis in Sec. II, the amplitude of the pressure gradient determined the oscillating acceleration amplitude of the liquid sheet. In the experiment, the three nozzle positions (VAN, IAN, and PAN) had different pressure gradients and reduced in turn; thus the atomization characteristics showed significant differences. The acoustic field of a form of standing wave is

$$p = \frac{1}{2} p_{ac} \cos(k_s x) \cos(\omega t). \quad (4.1)$$

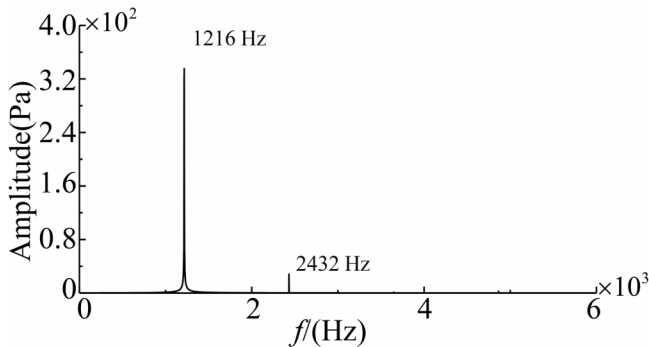


FIG. 8. Spectrum analysis diagram of microphone data.

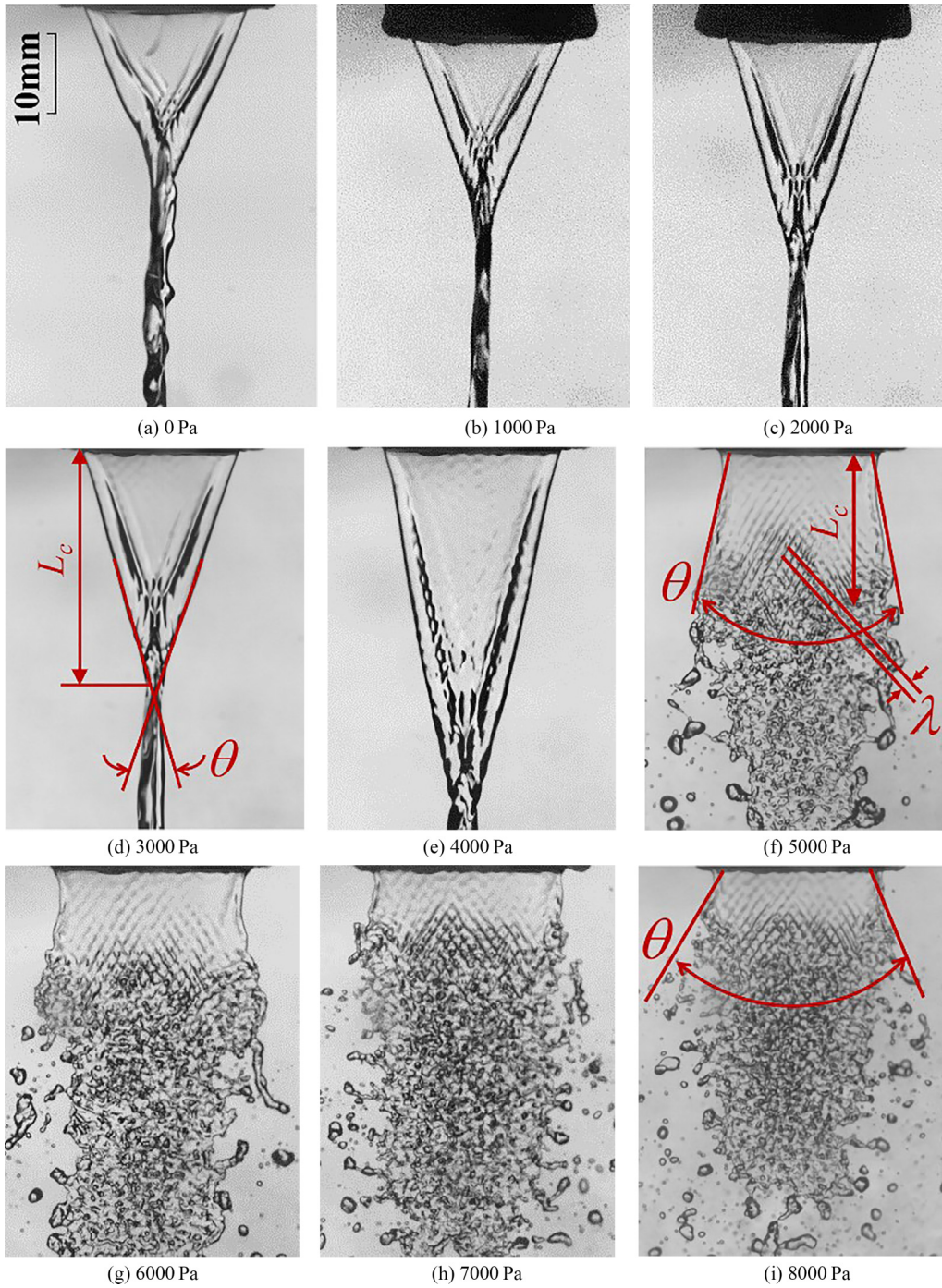


FIG. 9. Sheet behavior of the nozzle at VAN with different p_{ac} . The working condition corresponds to No. 1 shown in Table I. $f = 1216$ Hz.

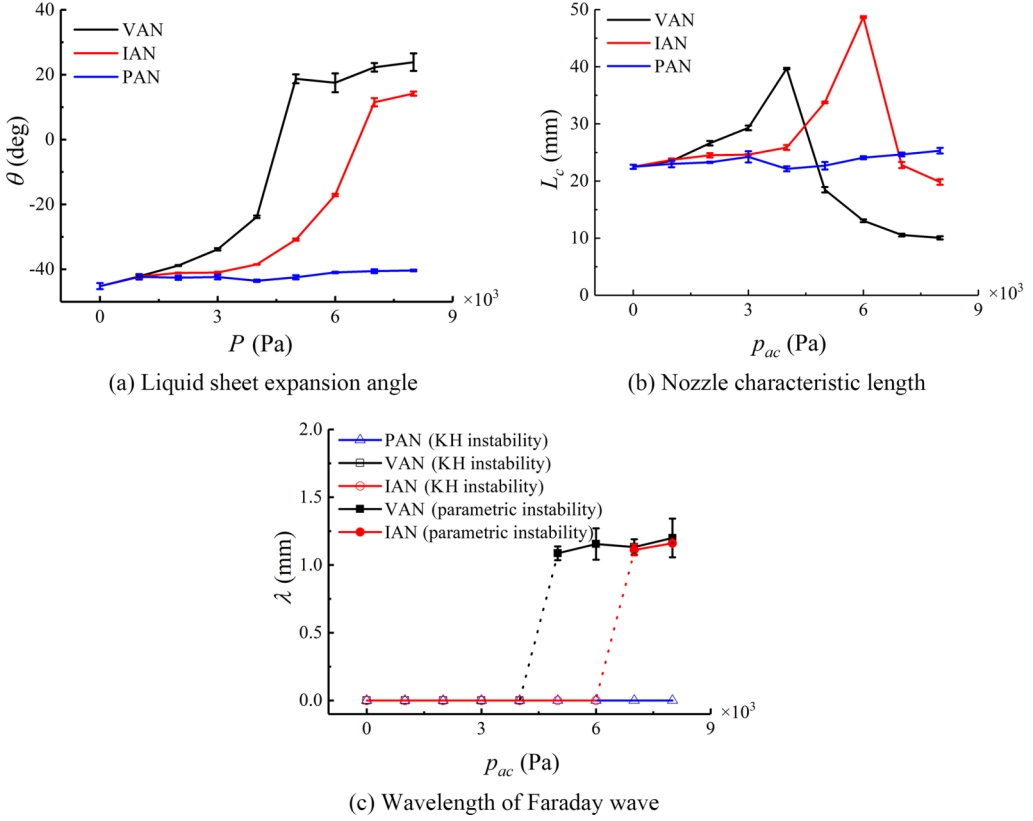


FIG. 10. Sheet behavior of the nozzle at VAN with different p_{ac} . The working condition corresponds to No. 1 shown in Table I. $f = 1216$ Hz.

Hence, the pressure gradient can be expressed as

$$\frac{\partial p}{\partial x} = -\frac{1}{2}k_s p_{ac} \sin(k_s x) \cos(\omega t) = F(x) \cos(\omega t), \quad (4.2)$$

where k_s is the wave number of the acoustic field, $F(x) = -k_s p_{ac} \sin(k_s x)$. At VAN, IAN, and PAN, the pressure gradient can be expressed as

$$\begin{aligned} |F[\frac{(1+2n)\pi}{2k_s}]| &= \frac{1}{2}k_s p_{ac}, & \text{VAN,} \\ |F[\frac{(1+2n)\pi}{4k_s}]| &= \frac{\sqrt{2}}{4}k_s p_{ac}, & \text{IAN} \\ |F(\frac{n\pi}{k_s})| &= 0, & \text{PAN.} \end{aligned} \quad (4.3)$$

Meanwhile, the thickness of the liquid sheet is $2a$, much smaller than the wavelength of the acoustic wave $2\pi/k$. Therefore, the pressure difference between the two surfaces is

$$\Delta p = \frac{1}{2}p_{ac} \{\cos[k_s(x+a)] - \cos[k_s(x-a)]\} \cos(\omega t) \approx 2aF(x) \cos(\omega t). \quad (4.4)$$

That is, the absolute value of $F(x)$ determines the pressure difference between the two surfaces. Obviously, Δp reaches its maximum value at VAN and its minimum value at PAN, explaining why the liquid sheet is most unstable at VAN and remains nearly unchanged at PAN, even though the sound pressure is very large, as shown in Fig. 13.

Figure 10 shows changes in the expansion angle θ , characteristic length L_c , and wavelength of the Faraday wave λ of the nozzle at VAN, IAN, and PAN with different p_{ac} . It can be concluded

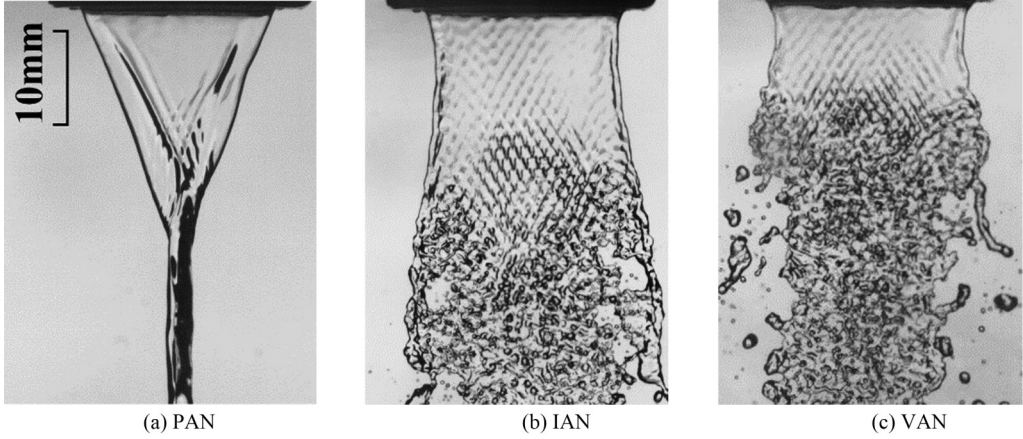


FIG. 11. Sheet behavior of the nozzle at different positions at $p_{ac} = 6000$ Pa. The working condition corresponds to No. 1 shown in Table I. $f = 1216$ Hz.

from Figs. 9 and 10 that, because of surface tension at VAN, the liquid sheet produced by the slit nozzle originally converged inward, and as p_{ac} increased, the liquid sheet was expanded under the effect of the acoustic field. Before the liquid sheet expanded (θ is negative), the breakup of the liquid sheet appeared as the edge impingement of the liquid sheet, forming a triangular liquid sheet with axis conversion. During this time, L_c increased with the increase of p_{ac} and reached maximum when the liquid sheet reached the critical state (θ is 0°). When p_{ac} exceeded the threshold of the critical pressure p_{cr} , the breakup of the liquid sheet appeared as the liquid sheet edge expanded, due to the effect of the acoustic field, forming a trapezoidal liquid sheet with Faraday waves on its surface. Note that the acoustic radiation pressure is a nonlinear effect of the acoustic field, which is proportional to p_{ac}^2 . The direction of acoustic radiation pressure is perpendicular to the liquid sheet and increases rapidly with the increase of sound pressure. The acoustic radiation pressure can overcome the surface tension at the rims of the liquid sheet, when p_{ac} exceeds a critical value. According to Baillot *et al.* [10,13], the acoustic radiation pressure can force the annular liquid jet into a liquid sheet. Similarly, the liquid sheet was expanded in the present experiment, parametric instability dominated the breakup of the liquid sheet, and under the action of oscillating sound pressure, the liquid sheet produced many small droplets, and atomization was very strong. During this time, L_c suddenly reduced, and gradually decreased with the increase of p_{ac} , while θ increased with increasing p_{ac} , but the increase of θ before p_{ac} reached the critical pressure was much faster than its state after p_{ac} exceeded the threshold. At IAN, as p_{ac} increased, L_c and θ displayed similar behavior as VAN, in general, but the value of critical pressure p_{cr} was higher than VAN. The critical acoustic pressure of the liquid sheet was in the range of 4000–5000 Pa at VAN, while it was 6000–7000 Pa at IAN. In the theory analysis in Eqs. (4.1)–(4.4), the amplitude of the pressure gradient determined the oscillating acceleration amplitude of the liquid sheet. In the standing wave acoustic field, the pressure gradient at VAN was $\sqrt{2}$ times as much as IAN, and the pressure gradient drove the liquid sheet to instability, but at PAN, the pressure gradient was zero, because the pressure on the two sides of the liquid sheet was equal, so the acoustic field could not drive the liquid sheet to oscillate at PAN. This was also the reasoning for the experiment in which the effect of the acoustic field was always strong at VAN, but the acoustic field had little effect at PAN. Returning to the critical acoustic pressure amplitude measured at VAN and IAN: The $\sqrt{2}$ times relationship between the two critical pressures also provided a basis for the instability analysis theory in this work. Section IV C compares and discusses the numerical applicability of the theory.

Figure 11 shows the atomization images of the nozzle at different positions with respect to the acoustic field when p_{ac} was 6000 Pa. It can be seen that, although the acoustic field changed the

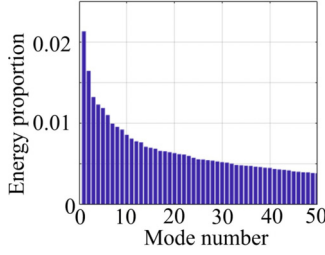


FIG. 12. Energy proportion distribution of different modes. The working condition corresponds to No. 1 shown in Table I. The liquid sheet locates at VAN. $p_{ac} = 6000$ Pa, $f = 1216$ Hz.

atomization state of the liquid sheet, under the same p_{ac} , the acoustic field had different effects on nozzles at different positions. Combined with Figs. 9, 10(a), and 10(b), it can be seen that at VAN, L_c and θ reached maximum, and among the three positions, the atomization of the nozzle was the most intense, while the effect of the acoustic field at IAN and PAN was reduced. Therefore, a conclusion can be made as the effect of the acoustic field weakened at VAN, IAN, and PAN in turn. It can be seen from Fig. 10(c) that with increased p_{ac} , λ generally increased. In addition, combined with Fig. 9, the generation of the Faraday wave appeared after the liquid sheet reached critical state.

Proper orthogonal decomposition (POD) [23] is a method that extracts information about experimental data by decomposing a complex signal into several simple orthogonal modes. The mode with the largest energy ratio is the dominant mode of the original signal and it represents the main feature of the signal. Using POD, the main characteristics of the instability of a liquid sheet formed by the slit nozzle (such as frequency and wavelength) can be extracted. Figures 12–14 are images obtained using POD on the liquid sheet at VAN when p_{ac} was 6000 Pa. The POD theory is described briefly below.

The high-speed camera can obtain 8-bit images; these images are the matrix that consists of a gray level of each pixel. Image A presents the transient information at time t , so the image $T(t)$ can be expressed as

$$T(t) = a^0(t)\varphi^0(x) + a^1(t)\varphi^1(x) + \dots, \quad (4.5)$$

where a^0, a^1, a^2, \dots are time coefficients at time t , and $\varphi^0, \varphi^1, \varphi^2, \dots$ are proper orthogonal modes (POMs). For a sequence of images, N is the quantity of the images, and $R \times C$ is the resolution of the images. Each image can be described by a matrix x^r , with a dimension $RC \times 1$, so the image sequence can be expressed as a matrix with the dimension $RC \times N$, where x^r represents the matrix

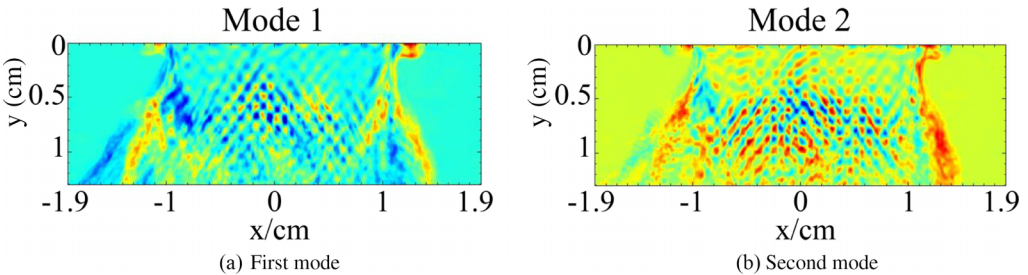


FIG. 13. Modes obtained with POD. The working condition is the same as that in Fig. 12.

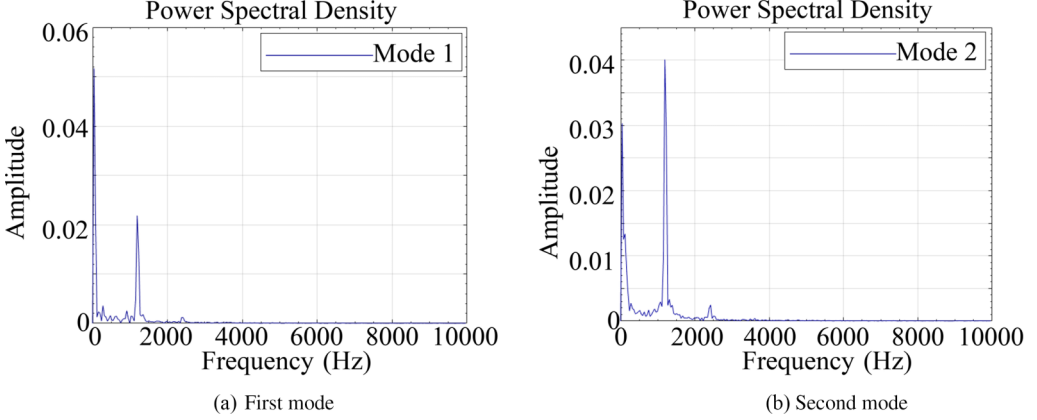


FIG. 14. Spectrum distribution of modes in POD. The working condition is the same as that in Fig. 12.

of the r^{th} image. The matrix can be expressed as

$$X = [x^1 \cdots x^N] = \begin{bmatrix} x_{1,1}^1 & \cdots & x_{1,1}^N \\ \vdots & \vdots & \vdots \\ x_{R,1}^1 & \cdots & x_{R,1}^N \\ x_{1,2}^1 & \cdots & x_{1,2}^N \\ \vdots & \vdots & \vdots \\ x_{R,2}^1 & \cdots & x_{R,2}^N \\ \vdots & \vdots & \vdots \\ x_{R,C}^1 & \cdots & x_{R,C}^N \end{bmatrix}. \quad (4.6)$$

Therefore, the average image is

$$\bar{x} = \frac{1}{N} \sum_{r=1}^N x^r, \quad (4.7)$$

and the matrix of pulsating quantity is

$$\hat{X} = X - \bar{X}. \quad (4.8)$$

Building up the matrix, we have

$$D = \hat{X}^T \hat{X}. \quad (4.9)$$

The eigenvectors A^i and eigenvalues λ^i can be obtained:

$$DA^i = \lambda^i A^i. \quad (4.10)$$

Sort the eigenvalues λ^i in descending order:

$$\lambda^1 \geq \lambda^2 \geq \cdots \geq \lambda^N, \quad (4.11)$$

so the energy ratio of each POM is

$$E_i = \frac{\lambda^i}{\sum_{j=1}^N \lambda^j}. \quad (4.12)$$

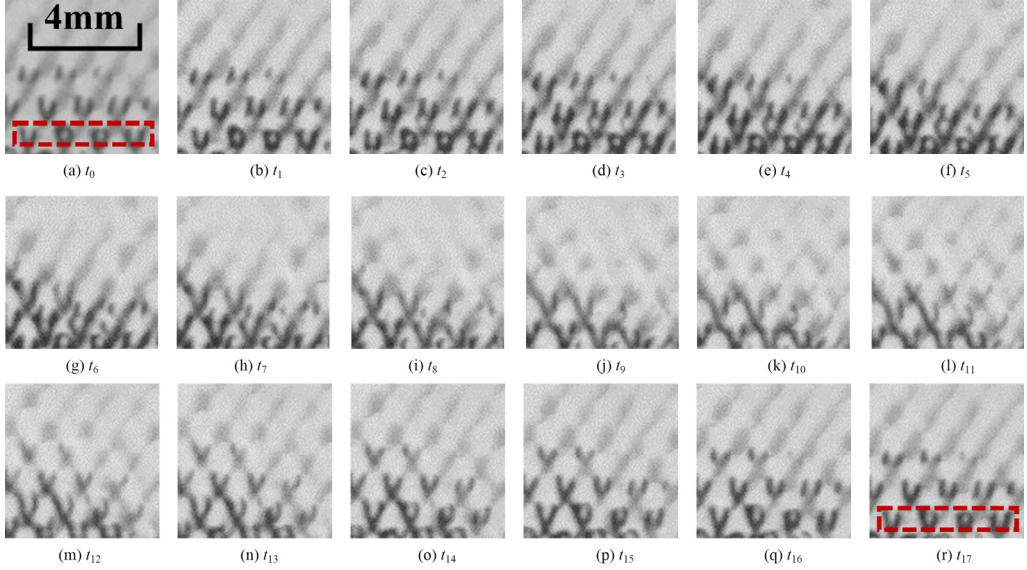


FIG. 15. Local image of the liquid sheet surface of a slit nozzle at different frames. $t_n = 5n \times 10^{-5}$ s. The working condition is the same as that in Fig. 12.

Then, the i th POM can be obtained:

$$\varphi^i = \frac{\sum_{n=1}^N A_n^i x^n}{\left\| \sum_{n=1}^N A_n^i x^n \right\|}. \quad (4.13)$$

Using 2000 continuous photos in the POD processing, the mode energy proportion distribution obtained is shown in Fig. 12. Among the different modes, the proportion of energy in the first few were much higher than the modes that followed. As shown in Fig. 13, the wavelengths of the first and second modes were equal, and the atomization form of the liquid sheet in the two modes matched in the experiment.

Figure 14 shows the spectrum analysis of the two modes in Fig. 13. It can be seen that the dominant frequency of the first and second modes was 1190 Hz—near the frequency of the acoustic field. In addition, Fig. 14 shows peaks close to 0 Hz in the spectrum of the two modes. The dominant frequencies corresponding to these two peaks was the frequency produced by the phenomenon of the Faraday wave traveling on the surface of the liquid sheet and oscillating at the same time. According to Fig. 4, the subharmonic region is the most unstable in the present experimental conditions. However, the frequency of the surface wave obtained by POD was equal to that of the acoustic field. This surface wave frequency could not be regarded as the frequency of the Faraday wave, which will be described in detail later.

Figure 15 shows the local atomization image at a fixed position of the liquid sheet at VAN when p_{ac} was 6000 Pa. It can be seen that, even though the Faraday wave was moving, its amplitude reached maximum when driven by the acoustic field (when the visual effect of the Faraday wave on the liquid sheet surface was most obvious); the peak and trough of the wave always appeared at the same spatial position. With this unique characteristic, it was inferred that the oscillating wave on the liquid face was a Faraday wave, and it was subharmonic.

As shown in Fig. 15, the black spots in the red box are the peaks and troughs in the interlacing Faraday wave region on the surface of the liquid sheet. In Fig. 15(r), the peaks and troughs of the Faraday waves appear for the second time at the same position. According to the time interval between the two figures, the frequency of this phenomenon was calculated as 1176 Hz—very close

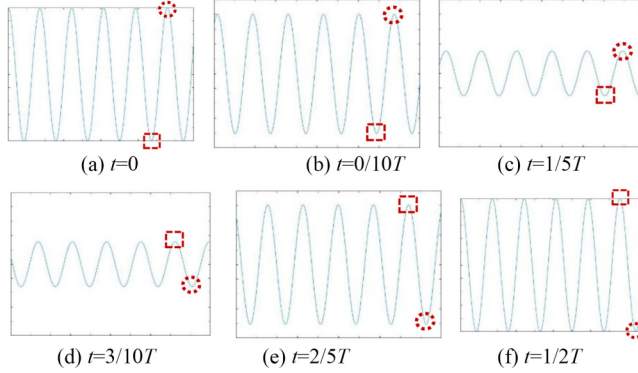


FIG. 16. Schematic diagram of a wave at a fixed spatial position traveling at the same frequency as the oscillating frequency of the Faraday wave.

to the oscillation frequency of the external acoustic field. At this high-frequency oscillation, the Faraday wave on the liquid sheet looked like an oscillating standing wave. It was not believed to be obtained directly from the oscillation frequency of the Faraday wave (which was proven by the subharmonic region of parametric instability in Fig. 15), because both the traveling frequency and the oscillating frequency of the wave must be considered. To illustrate the problem concisely: Assume that a wave W oscillates as it travels, the traveling frequency is ω_1 , and the oscillating frequency is ω_2 . In this case, the wave can be expressed by the following equation:

$$W = A \cos(kx + \omega_1 t) \cos(\omega_2 t), \quad (4.14)$$

where A is the amplitude of the wave and k is the wave number. Equation (4.14) can also be expressed as

$$W = \frac{A \cos [kx + (\omega_1 + \omega_2)t] + A \cos [kx + (\omega_1 - \omega_2)t]}{2}. \quad (4.15)$$

It can be seen in (4.15) that the peak and trough position of the wave was fixed in space only when $\omega_1 = \omega_2$. At this point, Eq. (4.15) can be simplified as

$$W = \frac{A \cos(kx + 2\omega_0 t) + A \cos(kx)}{2}, \quad (4.16)$$

where ω_0 is equal to the oscillating and traveling frequency of the wave.

Figure 16 shows a wave whose traveling frequency is equal to the oscillating frequency at different times in a fixed spatial position. After half a period, the peak of the wave moved to the trough at the initial moment, and its position was replaced by the upstream trough. Thus, when the peak and trough of the wave appeared at a fixed spatial position, the frequency obtained was actually twice that of the wave oscillating frequency. This also explains why the traveling wave observed from the image appears to be a standing wave, and the parametric instability region which occurred in the dispersion curve is a subharmonic region. The measured frequency in Fig. 15 was 1176 Hz, so the traveling and oscillating frequency of the Faraday wave was 588 Hz. Substituting the two frequencies into Eq. (4.16), two main frequencies were obtained after POD decomposition of the wave, one of which appeared near 1176 Hz. The other dominant frequency appeared near 0 Hz, which was also consistent with Fig. 14, proving the applicability of the parametric instability theory in this work.

Movies 1–4 (Supplemental Material [24]) illustrate the form of a traveling Faraday wave. It can be found that although the surface wave repeats four times in Movies 2–4, the Faraday wave travels only two wavelengths and the peaks and troughs transfers only two periods, indicating that the surface wave frequency is two times the traveling and oscillating frequency of the Faraday

TABLE II. The local velocity and thickness of the liquid sheet in the Faraday wave region.

Number	Flow rate (g/s)	Velocity (m/s)	Thickness (mm)
1	10.5	1.371	0.343
2	12.6	1.462	0.3221
3	14.7	1.7582	0.2675

wave. Moreover, Movie 4 displays superposition of the surface waves shown in Movies 2 and 3, qualitatively coinciding with the waveform in Movie 1 (see Supplemental Material [24]).

B. Effects of liquid Weber number

To explore the influence of the Weber number on the nozzle's atomization characteristics, an experiment was performed under conditions of numbers 1, 2, and 3, shown in Table I. The effect of nozzle flow rate was considered in the form of We_l .

While calculating the thickness of the liquid sheet, its morphology changed greatly under the acoustic field, so the width of the Faraday wave region and the local velocity were used to calculate the thickness of the liquid sheet. The local velocity was obtained by tracking the motion of the fluid in this region, in a short time, in the continuous images obtained during the experiment. Assuming that the cross section of the liquid sheet was rectangular, the thickness of the liquid sheet was calculated by combining the flow rate and the density of the working medium as follows:

$$2a = \frac{q}{\rho W U}, \quad (4.17)$$

where q , ρ , W , and U are the liquid mass flow rate, liquid density, width of the Faraday wave region, and the liquid velocity, respectively. These parameters can be obtained experimentally, and the local thickness of the liquid sheet can be obtained. The thicknesses for different cases are exhibited in Table II.

Figure 17 shows the atomization image of the slit nozzle at VAN with a different liquid Weber number when p_{ac} was 7000 Pa. In Fig. 18 the change of characteristic length, expansion angle, and wavelength of a Faraday wave by the liquid Weber number is shown when p_{ac} was 7000 Pa. Because the Faraday wave was affected by the surface tension and the inertial force of the liquid sheet, and because it occurred on the outside of the nozzle, the thickness of the sheet was chosen to receive the nondimensional wavelengths of the Faraday wave, which can be expressed as

$$\lambda^* = \frac{\lambda}{2a}. \quad (4.18)$$

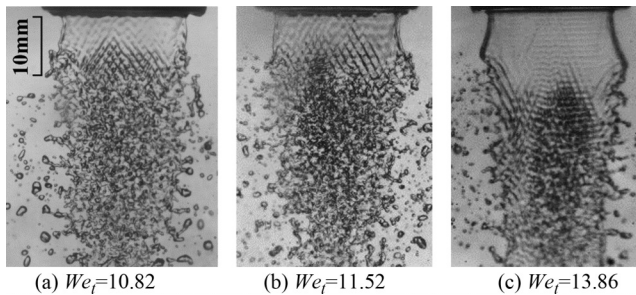


FIG. 17. Slit nozzle atomization at VAN when $p_{ac} = 7000$ Pa. $f = 1216$ Hz.

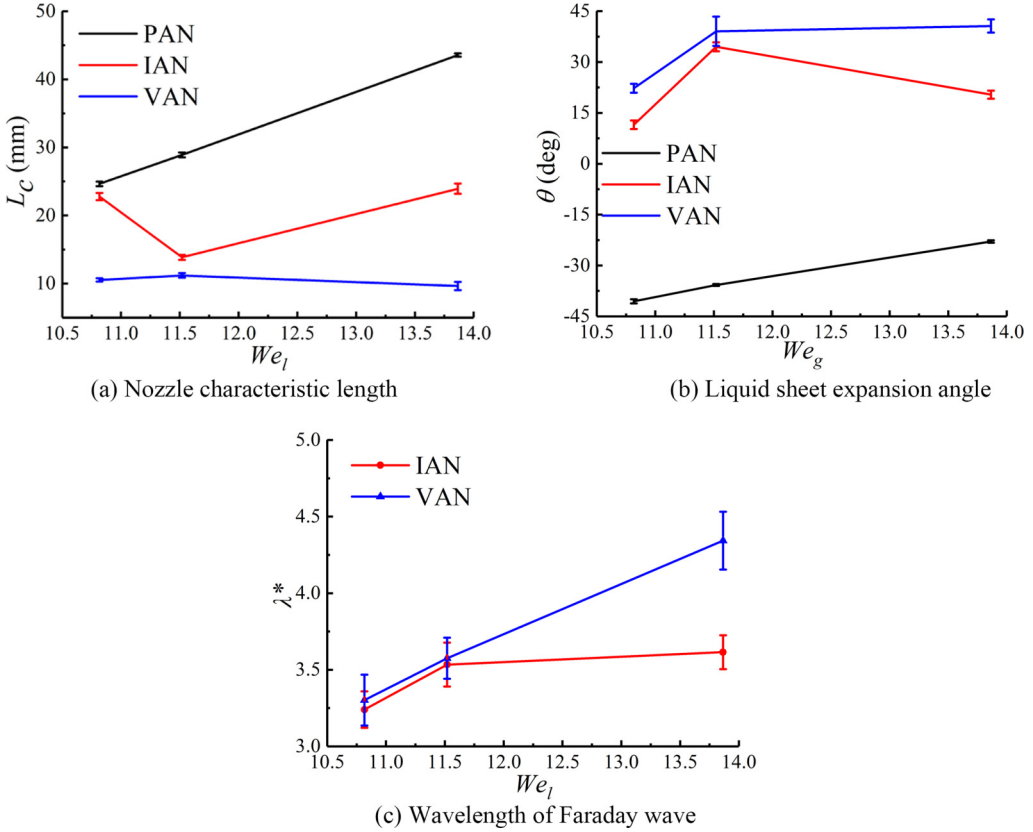


FIG. 18. L_c , θ , λ of nozzle at VAN, IAN, and PAN with different We_l when $p_{ac} = 7000$ Pa. $f = 1216$ Hz.

It can be seen from Figs. 17 and 18(b) that when the nozzle flow rate increased (that is, We_l increased), the expansion angle of the liquid sheet generally tended to increase when p_{ac} was 7000 Pa; this tendency was also applicable to other acoustic pressures in the experiment.

It can be seen in Fig. 18(a) that with the increase of We_l , at PAN, the characteristic length of the nozzle increased linearly, reflecting the increase in the nozzle flow rate. At VAN, the characteristic length of the nozzle did not change with We_l , which was also reflected in Fig. 17. It can be inferred that the influence of the acoustic field on the breakup of the liquid sheet reached a limit, and further increases in acoustic pressure would not significantly reduce the breakup length of the liquid sheet.

As seen in Fig. 18(c), the wavelength of the Faraday wave tended to increase with the increase of We_l when p_{ac} was 7000 Pa; this tendency is also applicable to other acoustic pressures in the experiment.

C. Verification and comparison of experiment with parameter instability analysis theory

In Secs. IV A and IV B, it was preliminarily confirmed that the parametric instability theory of a liquid sheet in a transverse standing wave acoustic field was suitable for the slit nozzle experiment in this work. The first section also proved that the oscillation frequency of the Faraday wave was subharmonic, like the parametric oscillation frequency from the dispersion curve in the theory. In this section, the critical acoustic pressure and the wavelength of the Faraday wave obtained from the experiment are quantitatively compared with the theory.

According to Eq. (2.10), the effect of the acoustic field was reflected by applying oscillating acceleration to the liquid sheet. The pressure difference ΔP between the two surfaces induced the

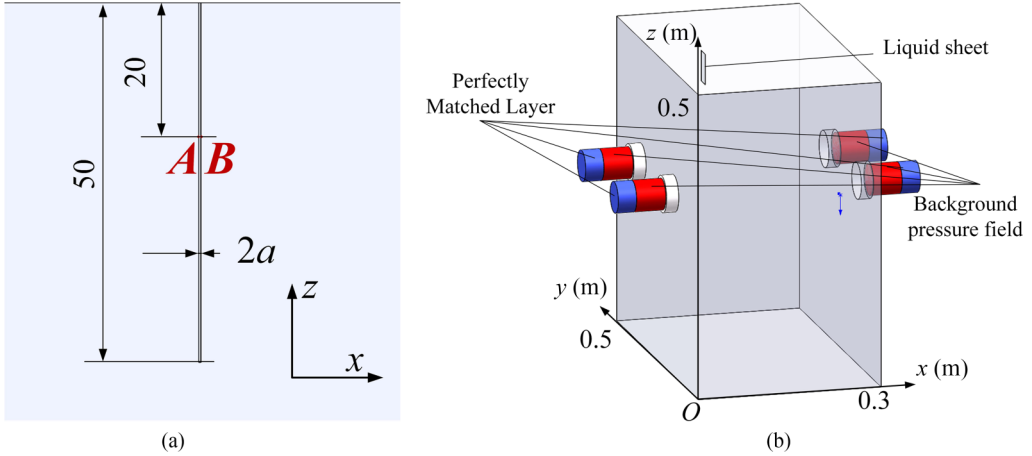


FIG. 19. The simulation domain of the sound field. (a) The size of the injector and the liquid sheet in the model, where A and B are points on the two surfaces of the liquid sheet. The medial surface of the liquid sheet locates at $x = 0.075$ m in all the cases studied. (b) The physical domain when the liquid sheet locates at VAN. The background pressure field is used to provide the in-phase pressured oscillations (P_s) of four loudspeakers. The boundaries of walls, the injector, and the liquid sheet are all set as sound hard boundaries (walls) except for the perfectly matched layer. The medium is set as air at 325 K.

oscillating acceleration of the liquid sheet, and the acceleration can be expressed as

$$g \cos(\omega t) = \frac{\Delta P}{\rho 2a} \cos(\omega t) = \frac{K p_{ac}}{\rho 2a} \cos(\omega t), \quad (4.19)$$

where K gives a linear relation between ΔP and p_{ac} . A brief numerical simulation was conducted to obtain K . The physical domain is 30 cm in length, 50 cm in width, and 50 cm in depth. Figure 19 displays the details of the simulation. COMSOL MULTIPHYSICS (version 6.0) was used to model, mesh, and analyze this system. The frequency domain was analyzed for different P_s . p_{ac} and ΔP were obtained according to the simulation.

A plane standing wave acoustic field is obtained when $f = 1204$ Hz, which agrees well with the experimental results. A cross section at $y = 0.25$ m is selected to investigate the pressure distribution in different cases, as shown in Fig. 20. The cross section passes through the center of the liquid

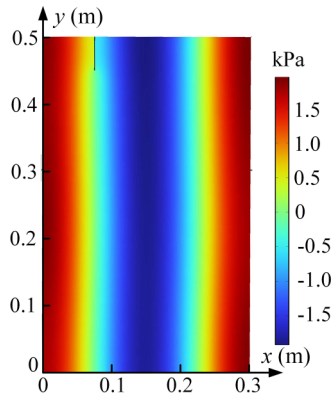


FIG. 20. The sound pressure distribution of the cross section $y = 0.25$ m when the sound pressure reaches its maximum. ($f = 1204$ Hz, $2a = 0.35$ mm, and $P_s = 1000$ Pa).

TABLE III. The pressure difference and K for different cases.

$2a$ (mm)	p_s (Pa)	p_{ac} (Pa)	p_A (Pa)	p_B (Pa)	ΔP (Pa)	$K (\Delta P / p_{ac})$
0.25	1000	3914.6	448.77	523.51	972.28	0.248
	1500	5872	673.15	785.27	1458.42	0.248
	2000	7829.4	897.54	1047	1944.54	0.248
	2500	9786.8	1121.9	1308.8	2430.7	0.248
0.30	1000	3918	450.41	525.76	976.17	0.249
	1500	5877	675.61	788.63	1464.24	0.249
	2000	7835.8	900.82	1051.5	1952.32	0.249
	2500	9794.8	1126.0	1314.4	2440.4	0.249
0.35	1000	3917.8	452.13	528.46	980.59	0.250
	1500	5876.8	678.19	792.69	1470.88	0.250
	2000	7835.8	904.25	1056.9	1961.15	0.250
	2500	9758.6	1130.3	1321.1	2451.4	0.251

sheet, so the pressure around the injector and the liquid sheet can be obtained. It can be found that the phase of the sound pressure is opposite on the two surfaces of the liquid sheet. Therefore, in Table III, $\Delta P = P_A + P_B$. It also can be found in Table III that K almost remains unchanged with the change of sheet thickness and P_s , because the thickness of the liquid sheet is much smaller than the acoustic wavelength. Therefore, K_1 was set as 0.249 at VAN. Using a similar method, K_2 was found to be 0.173 at IAN. $K_1/K_2 = 1.44 \approx \sqrt{2}$, which also coincides with the analysis of pressure gradients in Eqs. (4.1)–(4.4).

Figure 21 shows the critical state of the liquid sheet at VAN; the critical pressure corresponds to $p_{ac,cr} = 3200$ Pa. The liquid sheet expansion angle was nearly 0° , and Faraday waves began to appear on the liquid surface.

Figure 22 shows the growth rate varying with k and p_{ac} . It can be found that the theoretical critical pressure $p_{ac,cr} = 1741$ Pa. This critical pressure is much smaller than that measured experimentally. The reason is that when $p_{ac} < p_{ac,cr}$, the liquid sheet is not expanded, so the thickness of the liquid sheet is much larger than that shown in Table II. As a result, the acceleration was overestimated according to Eq. (4.19) when p_{ac} is relatively small. In the parametric instability region in Fig. 22,

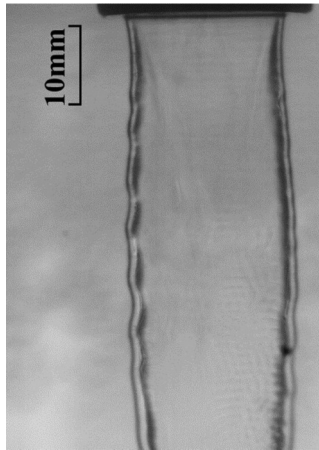


FIG. 21. Image of liquid sheet under critical acoustic pressure at VAN. The working condition corresponds to No. 3 shown in Table I. p_{cr} is between 3000 and 4000 Pa.

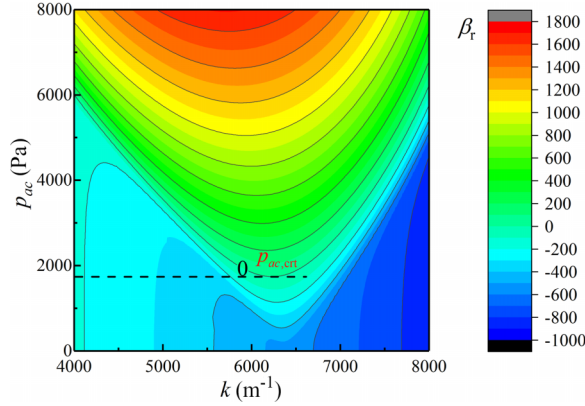


FIG. 22. The growth rate varying with k and p_{ac} . The working condition corresponds to No. 3 shown in Table I. $f = 1216$ Hz.

the wavelength of the Faraday wave was obtained by

$$\lambda = \frac{2\pi}{k_{\text{dom}}}, \quad (4.20)$$

where k_{dom} is the dominant wave number of the parametric instability region.

Figure 23 compares the theoretical wavelength of the Faraday wave [c calculated with the empirical coefficient $K_1 = 0.249$ (VAN) and $K_2 = 0.173$ (IAN)] and the measured wavelength of the Faraday wave in the experiment using different acoustic pressures at VAN and IAN. Figure 23(a) shows that the theoretical wavelength of the Faraday wave increased with increased acoustic pressure, which accords with the tendency of the dominant wave number varying with p_{ac} . The value of the wavelength calculated by the theory was in good agreement with that measured in the experiment. In Fig. 23(b), the theoretical wavelength of the Faraday wave also had the same tendency as in the experiment. In the experimental condition of Nos. 2 and 3 (Table I), Fig. 24 compares the theoretical wavelength of the Faraday wave [calculated with the empirical coefficient $K_1 = 0.249$ (VAN) and $K_2 = 0.173$ (IAN)] and the measured wavelength of the Faraday wave in the experiment with different acoustic pressures at VAN and IAN. The wavelength calculated by the theory was in good agreement with that measured in the experiment.

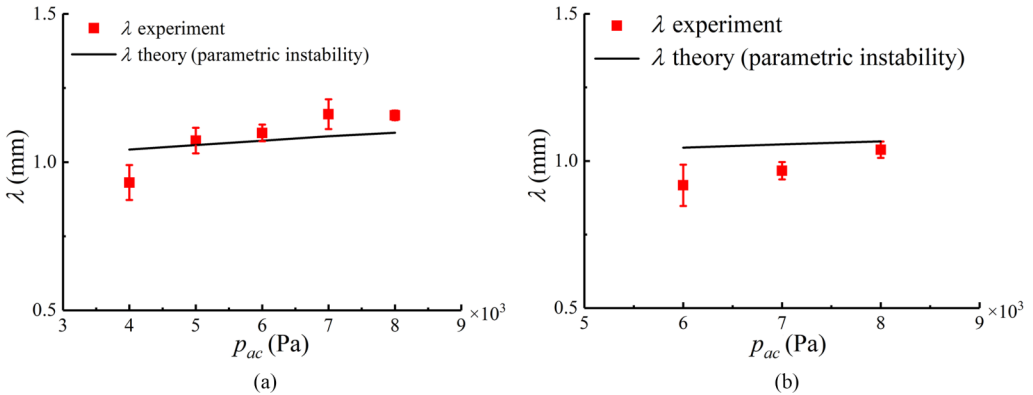


FIG. 23. Comparison of Faraday wavelength between experiment and theory: (a) nozzle at VAN; (b) nozzle at IAN. The working condition corresponds to No. 3 shown in Table I. $f = 1216$ Hz.

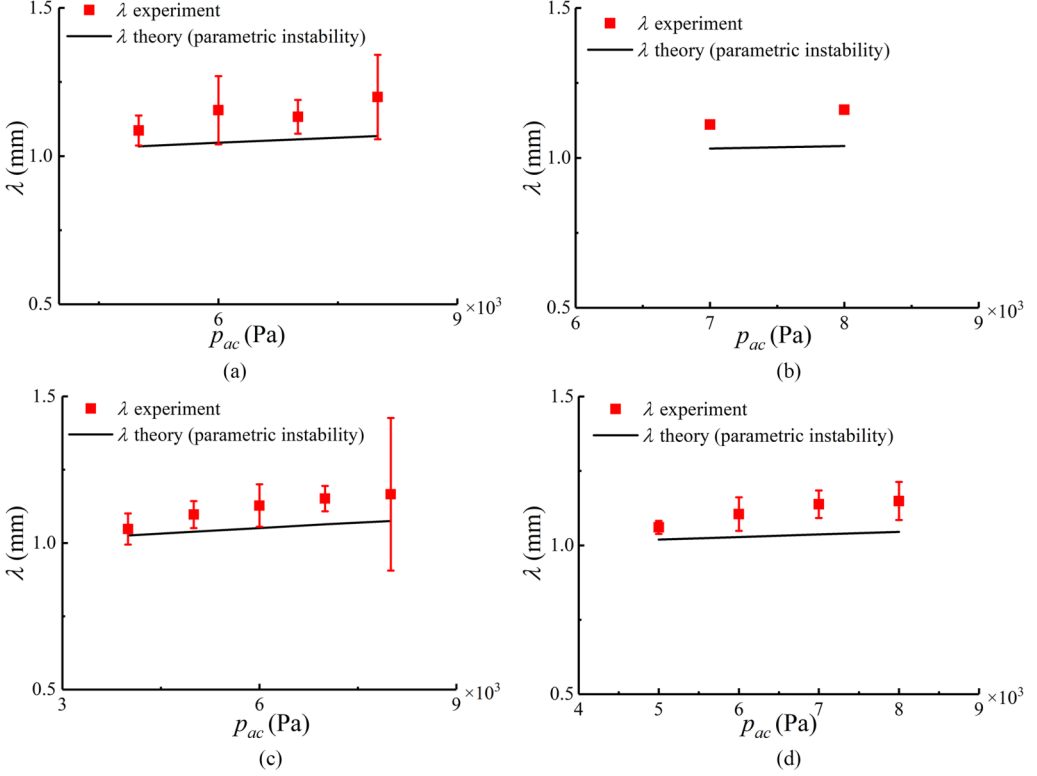


FIG. 24. Comparison between Faraday wavelength in the experiment and in theory. The working condition of (a), (b) corresponds to No. 1 shown in Table I, and the working condition of (c), (d) corresponds to No. 2 shown in Table I. $f = 1216$ Hz.

Except for the wavelength of the Faraday wave, the linear parametric instability analyses theory is suitable for the prediction of the breakup length of the liquid sheet. By choosing the suitable empirical coefficient [25], the breakup length of the liquid sheet l_{br} can be expressed as

$$l_{br} = \frac{U_0 \ln(2a/|\eta^-|)}{\omega_{r,max}}, \quad (4.21)$$

where $\ln(2a/|\eta^-|)$ is the empirical coefficient in predicting the breakup length.

Figure 25 compares the theoretical breakup length of the liquid sheet (calculated with the empirical coefficient $K_1 = 0.249$) and the measured breakup length of the liquid sheet in the experiment with different acoustic pressures at VAN. As shown in Fig. 25, the breakup length calculated by the theory decreased with the increase of p_{ac} , which agrees well with the experiment, indicating that the linear theory is able to obtain the tendency of the breakup length of the liquid sheet.

V. CONCLUSIONS

This work established the mathematical model of a liquid sheet under a transverse standing acoustic wave and obtained its dispersion relation. In the linear instability analysis, the varicose and sinuous modes were found to be coupled with each other. The increase of acoustic pressure amplitude enhanced parametric instability but restrained KH instability. In the subharmonic region, the interaction between the sinuous and varicose modes is the most dramatic.

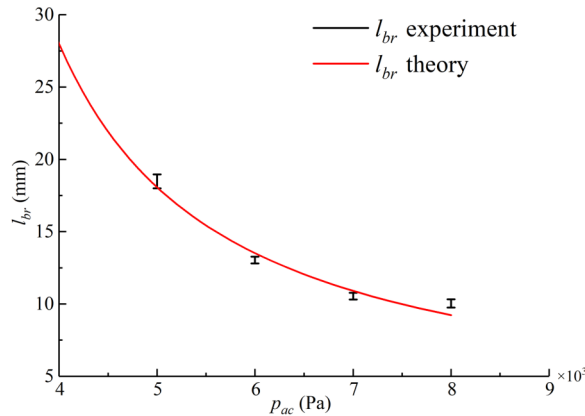


FIG. 25. Comparison of breakup length between experiment and theory for nozzle at VAN. The working condition corresponds to No.1 shown in Table I. $f = 1216$ Hz; $\ln(2a/|\eta^-|) = 8.75$.

The experiment examined the atomization characteristics of slit nozzles in a transverse standing wave acoustic field. At VAN of the acoustic field, the increase in acoustic pressure amplitude increased the expansion angle of the liquid sheet. In addition, the standing wave acoustic field also generated a Faraday wave on the liquid sheet surface. The surface wave frequency is the same as acoustic frequency, but the Faraday wave is subharmonic, because the surface wave frequency includes the influence of the traveling velocity of the Faraday wave.

Only when the acoustic pressure amplitude exceeded the critical acoustic pressure could the Faraday wave be motivated. Increasing acoustic pressure amplitude decreased the breakup length of the nozzle and increased the wavelength of the Faraday wave of the liquid sheet surface. At IAN of the acoustic field, atomization characteristics showed the same tendency as VAN, but the effect was weaker than VAN. At PAN, the acoustic field had little effect on the liquid sheet. The increase of the liquid Weber number increased the expansion angle, characteristic length, and the dimensionless wavelength of the Faraday wave of the liquid sheet.

At a specific flow rate, an empirical coefficient K exists, enabling it to predict the wavelength of Faraday wave and the breakup length of the liquid sheet using the linear instability theory.

ACKNOWLEDGMENTS

This work was supported by the National Natural Science Foundation of China (Grants No. 11872091, No. 11922201, and No. U1837211).

-
- [1] Liquid Rocket Engine Combustion Instability, edited by V. Yang and W. E. Anderson, *Progress in Astronautics and Aeronautics* (AIAA, Reston, VA, 1971).
 - [2] N. O. Rhys, Acoustic excitation and destruction of liquid sheets, Ph.D. thesis, The University of Alabama, 1999.
 - [3] V. Sivadas, E. C. Fernandes, and M. V. Heitor, Acoustically excited air-assisted liquid sheets, *Exp. Fluids* **34**, 736 (2003).
 - [4] V. Sivadas, Empirical correlation of the primary stability variable of liquid jet and liquid sheet under acoustic field, *J. Fluids Eng.* **138**, 084501 (2016).
 - [5] C. Siegler, A. Lozano, and F. Barreras, Application of an acoustic forcing on an air-blasted liquid sheet, in *Proceedings of 20th Annual Conference on Liquid Atomization and Spray Systems*, 2005, p. 215.

-
- [6] R. I. Sujith, An experimental investigation of interaction of sprays with acoustic fields, *Exp. Fluids* **38**, 576 (2005).
- [7] A. S. Mulmule, M. S. Tirumkudulu, and K. Ramamurthi, Instability of a moving liquid sheet in the presence of acoustic forcing, *Phys. Fluids* **22**, 022101 (2010).
- [8] S. Dighe and H. Gadgil, Dynamics of liquid sheet breakup in the presence of acoustic excitation, *Int. J. Multiphase Flow* **99**, 347 (2018).
- [9] S. Dighe and H. Gadgil, Atomization of acoustically forced liquid sheets, *J. Fluid Mech.* **880**, 653 (2019).
- [10] F. Baillot, Behaviour of an air-assisted jet submitted to a transverse high-frequency acoustic field, *J. Fluid Mech.* **640**, 305 (2009).
- [11] J. Carpentier, Behavior of cylindrical liquid jets evolving in a transverse acoustic field, *Phys. Fluids* **21**, 023601 (2009).
- [12] B. Chehroudi and D. Talley, Preliminary visualizations of acoustic waves interacting with subcritical and supercritical cryogenic jets, in *Proceedings of 15th Annual Conference on Liquid Atomization and Spray Systems* (ILASS Americas, Madison, Wisconsin, 2002).
- [13] A. Ficuciello, F. Baillot, J. B. Blaisot, C. Richard, and M. Theron, High amplitude acoustic field effects on air-assisted liquid jet, in *Proceedings of 52nd AIAA/SAE/ASEE Joint Propulsion Conference* (AIAA, Reston, VA, 2016), p. 5085.
- [14] A. Ficuciello, J. B. Blaisot, C. Richard, and F. Baillot, Investigation of air-assisted sprays submitted to high frequency transverse acoustic fields: Droplet clustering, *Phys. Fluids* **29**, 067103 (2017).
- [15] G. Taylor, The instability of liquid surface when accelerated in a direction perpendicular to their planes, *Proc. R. Soc. London, Ser. A* **201**, 192 (1950).
- [16] L. Kelvin, Influence of wind and capillarity on waves in water supposed frictionless, *Mathematical and Physical Papers (1871)* (Cambridge University Press, Cambridge, 1910), Vol. 42, p. 76.
- [17] T. B. Benjamin and F. Ursell, The stability of the plane free surface of a liquid in vertical periodic motion, *Proc. R. Soc. London, Ser. A* **225**, 505 (1954).
- [18] R. E. Kelly, The stability of an unsteady Kelvin-Helmholtz flow, *J. Fluid Mech.* **22**, 547 (1965).
- [19] K. Bauckhage, O. Andersen, S. Hansmann, W. Reich, and P. Schreckenber, Production of fine powders by ultrasonic standing wave atomization, *Powder Technol.* **86**, 77 (1996).
- [20] M. Faraday, On a peculiar class of acoustical figures, and on certain forms assumed by groups of particles upon vibrating elastic surfaces, *Philos. Trans. R. Soc. London* **121**, 299 (1831).
- [21] Z. Fang, T. Wang, B. Jia, L. Yang, Q. Fu, D. Sun, and X. Sun, Linear instability of a liquid sheet in a transverse standing acoustic field, *Phys. Fluids* **34**, 063310 (2022).
- [22] T. Poinso, C. L. Chatelier, S. M. Candel, and E. Esposito, Experimental determination of the reflection coefficient of a premixed flame in a duct, *J. Sound Vibr.* **107**, 265 (1986).
- [23] A. Chatterjee, An introduction to the proper orthogonal decomposition, *Curr. Sci.* **78**, 808 (2000).
- [24] See Supplemental Material at <http://link.aps.org/supplemental/10.1103/PhysRevFluids.7.124004> for a traveling Faraday wave.
- [25] L.-J. Yang, B.-Q. Jia, Q.-F. Fu, and Q. Yang, Stability of an air-assisted viscous liquid sheet in the presence of acoustic oscillations, *Eur. J. Mech. B: Fluids* **67**, 366 (2018).